An Emulator of Stratocumulus Cloud Response to Two Cloud-Controlling Factors Accounting for Internal Variability

Rachel W. N. Sansom[1] ⓘ, **Ken S. Carslaw[1]** ⓘ, **Jill S. Johnson[2]**, and **Lindsay Lee[3]**

[1]School of Earth and Environment, University of Leeds, Leeds, UK, [2]School of Mathematics and Statistics, University of Sheffield, Sheffield, UK, [3]Advanced Manufacturing Research Centre, University of Sheffield, Sheffield, UK

Abstract Large uncertainties persist in modeling shallow, low clouds because of many interacting nonlinear processes and multiple cloud-controlling environmental factors. In addition, sharp changes in behavior occur when environmental thresholds are met. Model studies that follow a traditional approach of exploring the effects of factors "one-at-a-time" are unable to capture interactions between factors. We simulate a stratocumulus cloud based on the Second Dynamics and Chemistry of Marine Stratocumulus field study using a large-eddy simulation model coupled with a two-moment cloud microphysics scheme. The simulations are used to train a Gaussian process emulator, which we then use to visualize the relationships between two cloud-controlling factors and domain-averaged cloud properties. Only 29 model simulations were required to train the emulators, which then predicted cloud properties at thousands of new combinations of the two factors. Emulator response surfaces of cloud liquid water path and cloud fraction show two behavioral regimes, one of thin and patchy yet steady stratocumulus and one of thick, growing stratocumulus with cloud fraction near 1. Internal variability (initial-condition uncertainty) creates unrealistic "bumpy" response surfaces. However, we show that the variability causing the bumpiness can be characterized in an emulator "nugget term" that is adjusted to match the distribution of a small number of initial-condition ensemble simulations at various points on the surface, thereby allowing a smoother, deterministic response surface to be constructed. Accounting for variability allows the transition between regimes, and the joint interactions of parameters, to be visualized in a more deterministic way that has not been done before.

Plain Language Summary Modeling shallow clouds is important because these clouds have an overall cooling effect on the planet, but the magnitude of this effect is very uncertain. Shallow cloud behaviors are made up of many interacting processes that work at a large range of scales, and we are not able to fully describe all these processes in large climate models. We use a machine learning technique called Gaussian process emulation to approximate output from the high-resolution cloud model so that we can study the cloud behavior at a much-reduced computational cost. By perturbing two cloud-controlling factors, we create a set of training data to train the emulator how to approximate the relationship between these factors and cloud properties of interest. We produce color maps that visually describe this relationship and we show that there are two regimes of cloud behavior. We assess the best way to account for cloud natural variability in the approximation. Gaussian process emulation is a vital tool for cloud modeling because it allows us to inspect whole cloud processes and the relationships between different inputs as they influence the output of interest. In this way we can better understand cloud processes and their uncertainties.

1. Introduction

Shallow, low clouds cover a larger area of the Earth than any other cloud type, with stratocumulus clouds alone covering one-fifth of the surface. They increase Earth's albedo in most regions because they reflect more solar radiation than the underlying surfaces (Wood, 2012), while having only a small effect on emission of terrestrial radiation. Therefore, globally, they have a net cooling effect (Hartmann et al., 1992). These clouds are important for the global radiation budget and how it changes over time in response to warming (cloud feedback: Bretherton, 2015; Ceppi et al., 2017; Schneider et al., 2019; Shen et al., 2022) and changes in aerosols (radiative forcing: Bellouin et al., 2020; Douglas & L'Ecuyer, 2020; Malavelle et al., 2017; J. Smith et al., 2020). However, their responses to changes in aerosols and the thermodynamic environment (cloud-controlling factors) are very uncertain (Myhre et al., 2013). Consequently the corresponding aerosol-cloud radiative forcing (Bellouin

et al., 2020; Lund et al., 2019; Seinfeld et al., 2016) and cloud feedbacks (Blossey et al., 2016; Bony & Dufresne, 2005; Nuijens & Siebesma, 2019; Zhang et al., 2013) are not well understood and significantly contribute to the uncertainties that persist in climate change projections (Dufresne & Bony, 2008; Peace et al., 2020). It is crucial that we efficiently use the modeling tools available to narrow this uncertainty in the outcomes of perturbations and climate feedbacks.

Much of the uncertainty in simulating clouds comes from the large number of interacting cloud-controlling factors. Key factors that affect the state and evolution of shallow clouds are local meteorology, large-scale forcings, radiative feedbacks and aerosols. Some of these factors, such as thermodynamic properties, can change on short timescales (hours) and shallow clouds respond quickly because internal changes in cloud microphysics and precipitation operate on similar timescales. Such cloud-controlling factors can have a dramatic effect on cloud properties, such as the rapid change from closed-to open-cell cloud structures (Stechmann & Hottovy, 2016). Other factors, such as large-scale divergence, operate on longer timescales and it can take 2–5 days for the cloud to adjust (Bellon & Stevens, 2013). Many of these factors covary and they also have joint effects on cloud processes, with counteracting effects creating a "buffered system" (Stevens & Feingold, 2009). In such a complex interacting system, changing one factor at a time to test cloud responses to various drivers cannot fully capture joint effects and interactions.

Our study has a similar focus to Dal Gesso et al. (2015), a model intercomparison that explored how stratocumulus cloud properties depend on two cloud-controlling factors (henceforth used interchangeably with "parameters"): the temperature and humidity differences between the surface and the free troposphere. The initial profiles of these factors were perturbed over a range of values at discrete Cartesian grid points across the 2-dimensional parameter space to study the effect on model outputs, such as cloud cover and liquid water content. This array of discrete model outputs across the parameter space allowed the model response to be partially visualized. However, this grid-point method restricts the information available from the simulation ensemble and, the number of simulations required to explore n factors also rises with 2^n. Additionally, as shown in Feingold et al. (2016), such a design of simulations may misrepresent the joint effects of factors.

To overcome the limitations of one-at-a-time sensitivity testing and to understand the joint effects of factors, we use Gaussian process emulation to generate "response surfaces" that describe how cloud properties respond to the joint effects of multiple cloud-controlling factors. Gaussian process emulation is a machine learning method to approximate the relationship between a set of model input parameters and a model output (O'Hagan, 2006). Compared to other machine learning methods, this requires only a small number of well-designed model simulations as training data. The emulator function (the approximated relationship between model outputs and inputs) can then be sampled millions of times at a fraction of the computational cost of running the model for the equivalent points in parameter space. From this dense sampling, we can produce a response surface with an associated uncertainty at any point in parameter space. The power of emulation is in the ability to study how large numbers of parameters interact to influence the output of interest and also to visualize all combinations of parameters within their realistic ranges at comparatively low computational cost. In previous emulation work, the parameters were often related to uncertain processes in the model, but here the parameters are cloud-controlling factors.

Gaussian process emulation has been widely applied in aerosol and aerosol-cloud science. First, response surfaces are an effective tool for visualizing the combined effects of the uncertain input parameters and an output of interest, such as in Marshall et al. (2019, 2021) for volcanic eruptions. Transformations from parameter space to state space (Glassmeier et al., 2019; Hoffmann et al., 2020) or selection of a few key parameters at once allows higher dimensions to be visualized (Lee et al., 2011). Second, variance-based sensitivity analysis based on a large number of emulator data points rather than the sparse training data is used to understand which parameters contribute most to the variance in the output of interest (Johnson et al., 2015; Lee et al., 2011, 2013; Regayre et al., 2014, 2015, 2018; Saltelli et al., 2000). Third, the uncertain parameter ranges can be constrained using observations of the model outputs (Johnson et al., 2018; Marshall et al., 2021; Regayre et al., 2018, 2020), which can lead to constraint of additional outputs for which observations are not available.

The first cloud model emulation study was Johnson et al. (2015). They perturbed initial aerosol concentrations and nine microphysical model parameters in a deep convective cloud microphysics model. Sensitivity analysis showed that the cloud properties considered were most sensitive to aerosol concentrations and graupel collection efficiency. This demonstrated the insight that can be gained from emulating cloud models, where buffering can

obscure relationships between input parameters and cloud responses. Perturbing multiple input parameters together reveals how they jointly affect an output and under what conditions certain parameters have a larger effect than others. Following this work, emulation has been used to analyze the sensitivity of deep convective cloud properties (Wellmann et al., 2018, 2020) and sea breeze convection (Igel et al., 2018; J. M. Park et al., 2020) to initial meteorological conditions. Additionally, Glassmeier et al. (2019) and Hoffmann et al. (2020) have used emulation of state variables to explore cloud-processes in stratocumulus. Here, we use emulation to study the covariance of initial meteorological conditions in stratocumulus and, like Johnson et al. (2015) and J. M. Park et al. (2020), we identify regimes of cloud behavior in parameter space.

Shallow clouds often display sharp changes in behavior (between regimes) as cloud-controlling factors change. This can make Gaussian process emulation challenging because of the required assumptions about smoothness. Feingold et al. (2016) found a steep gradient in a study of nocturnal marine stratocumulus clouds in which six parameters were perturbed. Pope et al. (2021) demonstrated that the steep gradient in this data set could be emulated using a non-stationary method, where Voronoi tessellations defined regions of the 6-dimensional parameter space where separate, stationary emulators could be applied, which followed the assumption of smoothness. The discontinuity was primarily caused by perturbations in aerosol concentration, but the high dimensionality of the parameter space made visualizing the discontinuity difficult. Here, we have visualized a steep gradient in two dimensions and used adaptive sampling to explore it, but we found that it emulates reasonably so stationary methods sufficed.

Another challenge in visualizing cloud behavior as a response surface is that some cloud models exhibit a high degree of internal variability, which may obscure the deterministic behavior that an emulator is designed to represent. In a purely deterministic model, the emulator function should interpolate exactly through all the training data. However, due to the nonlinear processes within cloud models, a small change in the initial conditions can lead to much larger changes later in the simulation, making the cloud properties highly dependent on the initial conditions used for the simulations at each point in parameter space. Internal variability can be averaged out by running initial-condition ensembles at each point in parameter space and using the ensemble mean as training data (Henderson et al., 2009; Johnson et al., 2011; Oyebamiji et al., 2017). For global climate models, which are resource intensive, this variability is usually estimated using maximum likelihood methods (Pope et al., 2021; Williamson & Blaker, 2014). Here, we show that the internal variability of our cloud model can be approximated based on initial-condition ensembles at just a few points in parameter space.

In this study, we assess the ability of statistical emulation to capture the transition between two regimes of shallow cloud behavior as initial vertical profiles of two cloud-controlling factors (parameters) are varied. We then explore a method to quantify internal variability and account for it when training emulators. We start from a homogeneous stratocumulus-topped boundary layer that has steady cloud properties despite environmental conditions that make the cloud prone to breaking up, as hypothesized by Lilly (1968), Randall (1980) and Deardorff (1980), before Mellado (2017) later concluded that such cloud break up is not so distinct. Two parameters are perturbed to identify where cloud breakup does occur across the parameter space. We will answer the following questions. First, how well can we characterize the change in cloud behavior using statistical emulation? Second, can we visualize the transition between regimes to discern how distinct they are? Third, how can we account for the model's internal variability in the emulators so that the response surfaces represent deterministic cloud behavior rather than single realizations of nonlinear processes?

The remainder of this paper is laid out as follows. Section 2 gives context to the cloud-breakup region and Section 3 describes the model simulation setup, the initial simulation and the parameter perturbations. Section 4 discusses the cloud behavior displayed across the perturbed parameter ensemble (PPE) and exploring the model's behavior around the cloud-breakup threshold. The model's internal variability will be quantified and included in the emulation method in Section 5. The results are discussed further in Section 6.

2. Theoretical Context

The simulations are based on observations from the first research flight (RF01) of the Second Dynamics and Chemistry of Marine Stratocumulus field study (DYCOMS-II) (Stevens et al., 2003), which took place off the west coast of California in July 2001. Flight RF01 observed a homogeneous, non-drizzling stratocumulus cloud deck over 9 hr through the night. Dropsondes measured a well-mixed boundary layer up to 850 m initially, but the boundary layer and cloud layer deepened by 50 m over the course of the flight, resulting in a 250 m thick cloud.

The well-mixed stratocumulus-topped boundary layer was capped by a temperature inversion, where the potential temperature, θ, increased by 8.5 K and the total water mass mixing ratio, q_t, decreased by 7.5 g kg^{-1} within a few tens of meters of cloud top.

Stevens et al. (2005) conducted a large-eddy simulation (LES) model intercomparison study based on RF01 to compare 10 models. Many of the models simulated a more broken cloud than observed, with lower cloud fraction and lower liquid water path (the vertically integrated liquid water content), and some simulated boundary layer decoupling, which was not observed. A decoupled boundary layer is no longer well-mixed and cloud water content tends to decrease because ocean moisture no longer reaches the cloud layer. Stevens et al. (2005) suggested that differences between the models and observations might partially be because the temperature and humidity properties of the inversion made the simulations particularly sensitive to a cloud-dissipating mechanism, cloud-top entrainment instability, described below. Other LES studies that have simulated DYCOMS-II RF01 generally fall within the multi-model range of the intercomparison study (Ghonima et al., 2015; Pressel et al., 2017; Xiao et al., 2011; Yamaguchi & Randall, 2008).

The stratocumulus-topped marine boundary layer can persist as a uniform cloud field for days before transitioning to a cumulus state or breaking up (sometimes entirely) within a couple of hours. Lilly (1968) proposed a theoretical mechanism for this rapid change where warm, dry air mixed into the cloud from above (entrainment) leads to evaporative cooling and enhanced mixing, which may create a positive feedback that can rapidly dissipate the cloud. Mellado (2017) summarized recent studies that found the feedback is not strong enough under realistic conditions to dissipate marine stratocumulus clouds, especially alongside other confounding factors.

Randall (1980) and Deardorff (1980) derived an inversion instability parameter, κ, with a threshold beyond which the cloud-dissipating feedback occurs,

$$\kappa = 1 + \frac{c_p}{L_v} \frac{\Delta \theta_l}{\Delta q_t},$$ (1)

where c_p is the specific heat of air, L_v is the latent heat of vapourization, $\Delta \theta_l$ and Δq_t are the changes in potential temperature (for liquid water) and in total water mass mixing ratio, both at the inversion. Van Der Dussen et al. (2014) summarized the Randall and Deardorff criterion as $\kappa = 0.23$, which we use as the threshold value here. Several studies have improved on this derivation and mapped out the dependence of κ on these two parameters, $\Delta \theta_l$ and Δq_t, using one-at-a-time model sensitivity simulations (Dal Gesso et al., 2015; Kuo & Schubert, 1988; MacVean & Mason, 1990; Siems et al., 1990; Van Der Dussen et al., 2014; Xiao et al., 2011; Yamaguchi & Randall, 2008).

Here we simulate DYCOMS-II RF01 and perturb $\Delta \theta_l$ and Δq_t across a range of values to map out cloud behavior in their joint parameter space and visualize the transition to a degree that has not been done before.

3. Experiment Design

3.1. Model Description

The LES model used here is the UK Met Office/Natural Environment Research Council (NERC) Cloud (MONC) model (N. Brown et al., 2020). All simulations were nocturnal and used the longwave cooling parameterization used in Stevens et al. (2005) and Ackerman et al. (2009), which calculates the net upward longwave flux from the liquid water mass mixing ratio profile and several tuning parameters, for which we have used the same values as in Stevens et al. (2005). Horizontal resolution was 30 m and vertical resolution varied between 7.5 m around the inversion and 10–20 m elsewhere in the boundary layer. The domain size was 250 by 250 grid boxes with 110 vertical layers up to 1,500 m. The subgrid mixing scheme for unresolved turbulence, diffusion and viscosity is an extension of the Smagorinsky-Lilly model (detailed in A. R. Brown et al., 1994).

The microphysics scheme used is the Cloud AeroSol Interacting Microphysics (CASIM) model, which is a bulk scheme that can use up to three moments for each hydrometeor (Dearden et al., 2018; Field et al., 2023; Hill et al., 2015; Shipway & Hill, 2012). Here we define cloud liquid and rain droplets by two moments: number concentration and mass mixing ratio.

The particle size distribution is defined as,
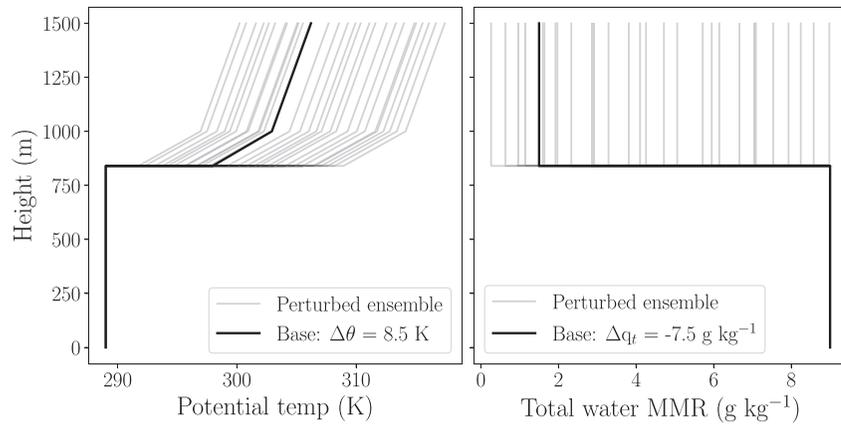
Figure 1. Initial profiles of potential temperature and total water mass mixing ratio for all simulations. Solid lines show the base simulation values taken from the DYCOMS-II observational campaign flight RF01, while gray lines show the profiles for the perturbed parameter ensemble members.

$$N(r) = N_0 r^\mu e^{-\gamma r}, \tag{2}$$

where r is a measure of size, N_0 is the distribution intercept parameter, μ is the shape parameter and γ is the slope parameter (Shipway & Hill, 2012). The kth moment is then defined by,

$$M_k = \int r^k N(r) dr, \tag{3}$$

giving the number concentration (zeroth moment) as $M_0 = N_0$ and the mass mixing ratio (third moment) is $M_3 = \frac{4}{3}\pi r^3 N_0 \exp\left(\frac{9}{2}\ln^2 \sigma\right)$ for a lognormal distribution.

Condensation and evaporation were calculated by a saturation adjustment scheme, where any surplus water vapor in the cloud condenses onto the fixed number of cloud droplets and any deficit evaporates from the droplets, keeping the relative humidity within the cloud at 100%. Cloud droplets can be autoconverted and collected into rain droplets, and rain droplets can precipitate and either reach the surface or evaporate in sub-saturated air below the cloud base. Condensation of water vapor onto rain cannot occur due to the saturation adjustment scheme (Gray et al., 2001). Sedimentation was switched on for both cloud droplets and rain, which advects water mass downwards through the boundary layer. Autoconversion and collection are dependent on cloud water mass mixing ratio, rain water mass mixing ratio and droplet number concentration (Khairoutdinov & Kogan, 2000). New air is homogeneously mixed from above the cloud into the cloud layer, which means clear air is mixed into the cloudy air before evaporation is calculated so all droplets are evaporated equally until saturation is reached. Thus, there is a reduction in cloud droplet radius, but cloud droplet number is not affected.

3.2. Perturbed Parameter Ensemble

A base simulation was initialized to match the DYCOMS-II RF01 setup in Stevens et al. (2005). The simulation was run for 8 hr with initial surface sensible and latent heat fluxes of 15 W m^{-2} and 115 W m^{-2}. The initial profiles of θ and q$_t$ are shown in Figure 1.

We perturbed the initial $\Delta\theta$ and Δq_t to explore the joint effect of these two parameters, creating a perturbed parameter ensemble (PPE) in the 2-dimensional parameter space (Figure 1). The initial profiles were kept the same up to the inversion at 840 m, where the magnitude of the jump was varied for both. The ranges for these parameters were chosen based on the ranges outlined in Van Der Dussen et al. (2014):

$$2 \text{ K} \leq \quad \Delta\theta \quad \leq 20 \text{ K} \tag{4}$$

$$-9 \text{ g kg}^{-1} \leq \quad \Delta q_t \quad \leq 0 \text{ g kg}^{-1}. \tag{5}$$
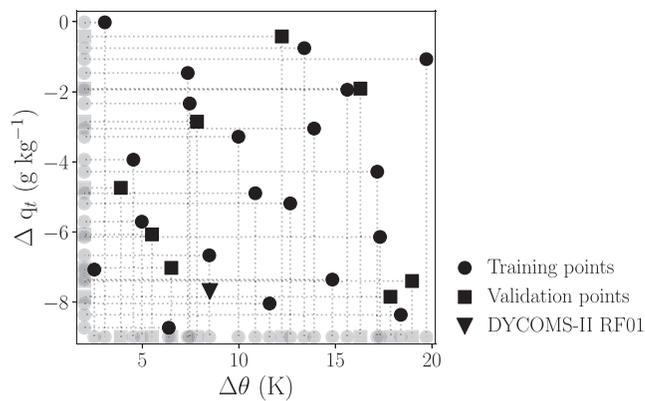
Figure 2. Latin hypercube design for the PPE. Circles show training points and squares show validation points. Faded markers show the distribution along each dimension. The triangle marker is the base simulation.

Theoretically, cloud thickening occurs for conditions below the κ threshold which is in the region of parameter space where $\Delta\theta \rightarrow 20$ K and $\Delta q_t \rightarrow 0$ g kg^{-1}. Cloud thinning occurs above the κ threshold where $\Delta\theta \rightarrow 2$ K and $\Delta q_t \rightarrow -9$ g kg^{-1}. For a cloud fraction ≈ 1, cloud thickening is roughly analogous to an increasing liquid water path throughout the simulation—a positive liquid water path tendency.

The PPE simulation data were used as training data for Gaussian process emulation. The combinations of joint values of $\Delta\theta$ and Δq_t were defined using a "maximin" Latin hypercube algorithm comprised of 20 simulations, which has been shown to be sufficient to create an emulator over a 2-dimensional parameter space (Lee et al., 2011; Loeppky et al., 2009; Morris & Mitchell, 1995). The Latin hypercube (Figure 2) is a space-filling design that samples the parameter space efficiently to provide as much information as possible about the model to an emulator. In comparison, regular gridded (Cartesian) designs are an inefficient way of sampling a high-dimensional space. This becomes crucial if the sensitivity to some parameter perturbations is much greater than for others. When this type of design is projected to lower dimensions, as in Figure 2, design points are not replicated.

Although the 20-member PPE was sufficient for training an emulator, it lacked data around the particular region of interest. As will be shown later, the PPE was supplemented by six additional training points to sample near the κ threshold and areas where more extreme model output values were observed.

3.3. Gaussian Process Emulation

Gaussian process emulation is a Bayesian statistical approach to generate a mapping between a multi-dimensional input space (the parameters) and an output of interest (O'Hagan, 2006). This mapping can be used to predict the model's output for thousands of new parameter input combinations at a considerably reduced computational cost. It requires training data, consisting of input settings and corresponding output data from multiple model simulations over the perturbed parameter ranges. Under the Bayesian paradigm, the approach is initiated with a prior Gaussian process specification for this mapping, which encapsulates any prior knowledge about the model output. The prior is updated using the training data to create a better estimation of the function representing the model output response (also of Gaussian form) to the perturbed inputs. This better estimation is a posterior Gaussian process specification, and is our emulator which can be thoroughly sampled. The uncertainty surrounding each emulator-predicted output value is also calculated assuming a Gaussian error structure and based on proximity to the training data. A second smaller set of simulations is used to validate the emulator to ensure that it is producing a reasonable representation of the model's behavior.

For constructing the emulator, the prior consisted of a linear mean function and the Matérn $\frac{5}{2}$ covariance structure. The Matérn covariance structures have been found to work well for rougher output. All emulation processes were calculated using the "km" function of the DiceKriging package (Roustant et al., 2012) in R (R Core Team, 2018). The emulator fit is described by a set of hyperparameters, which are difficult to specify in the prior so they are estimated from the training data within the "km" function. Initial values are estimated and then optimized using the Broyden–Fletcher–Goldfarb–Shanno algorithm (Fletcher, 1987) to maximize the marginal likelihood function (J.-S. Park & Baek, 2001; Rasmussen & Williams, 2006). Our estimation of the nugget term, introduced in Section 5, is compared to the in-built estimation of the nugget term using this maximum likelihood estimation (MLE). A validation data set consisting of eight additional simulations was created by augmenting the 20-point Latin hypercube design.

4. Results

We focus on the response of in-cloud liquid water path and cloud fraction to perturbations in cloud-controlling factors. The cloud fraction is the fraction of columns with liquid water content greater than 0.01 g m^{-3}. The liquid water path and cloud fraction values are calculated as domain means over the final 2 hr of simulation time. The
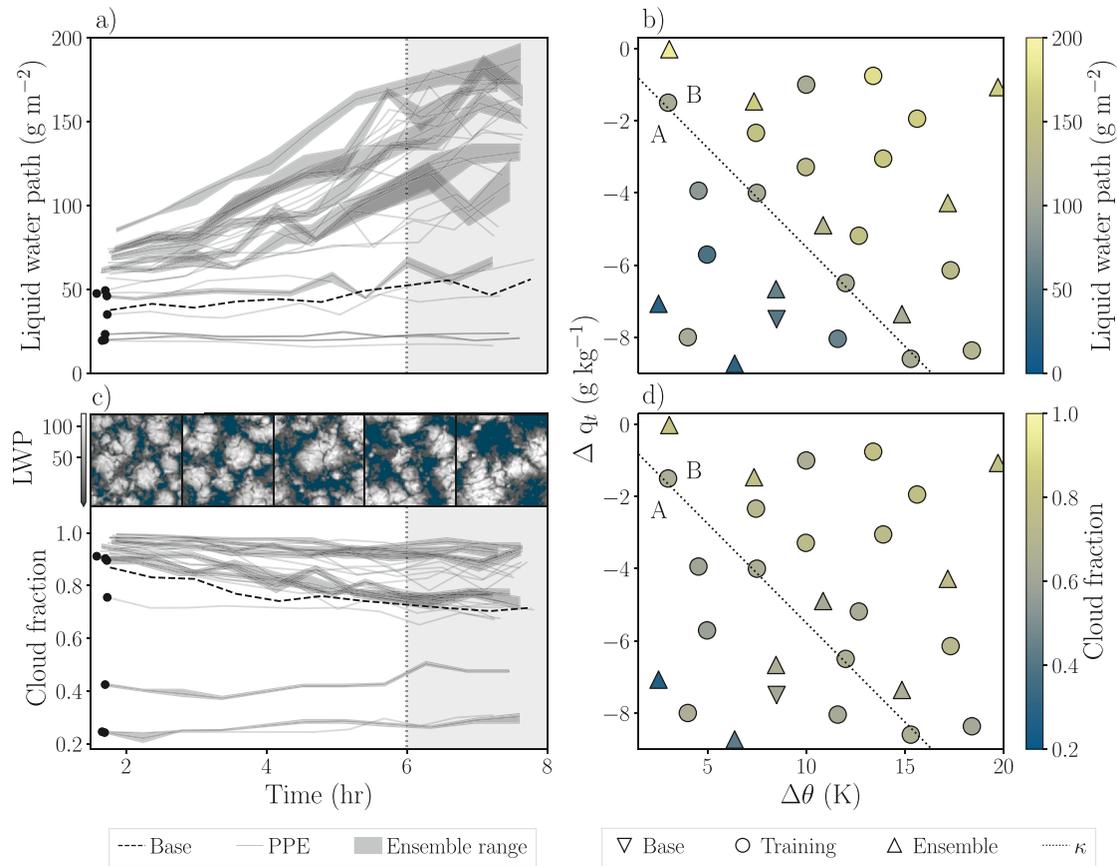
Figure 3. PPE model output. Liquid water path (a) timeseries post-spinup to the end of the simulation, the last 2 hr of which is averaged (shaded area) to produce (b) the training data in joint parameter space, $\Delta\theta$ versus Δq_t. Cloud fraction (c) timeseries and (d) training data. The inset in panel (c) shows top-down snapshots of the liquid water path for the base simulation. The κ line is the theoretical threshold described in Section 2, which splits the regions into A and B. Simulations from region A are marked in panels (a, c) with a black dot at the beginning. Initial-condition ensembles, discussed in Section 5, were run at a selection of training points. The spread of these ensembles is shown by the shaded ensemble range and their locations in parameter space by the upright triangles.

tendencies of both are the rates of change over the remaining 6 hr of simulation time, after the 1.5-hr spin-up period.

4.1. Base Case Simulation

The base simulation has mean liquid water path, L, of 38 g m^{-2} (Figure 3a), similar to the multi-model mean in Stevens et al. (2005) of 40 g m^{-2}. The top-down liquid water path snapshots in Figure 3c (inset) show that the cloud initializes as homogeneous stratocumulus and the cells grow and thicken slightly over 6 hr. The cloud boundaries are mostly constant during the simulation, with cloud base at around 600 m and cloud top at 840 m. L increases through the simulation up to 56 g m^{-2}, so the L tendency is 2.2 g m^{-2} hr^{-1}, whereas it is slightly negative in Stevens et al. (2005). Cloud fraction, f_c, starts at 0.87 (Figure 3c) and decreases to 0.72 giving a f_c tendency of -0.02 hr^{-1}. The initial f_c is in the lowest quartile of the multi-model range in Stevens et al. (2005). The multi-model mean f_c begins near 1 and decreases to approximately 0.8, with the majority following similar behavior, but a small number of models simulated a decrease to around 0.2.

4.2. Perturbed Cloud Behavior

Figures 3a and 3c show that there is considerable spread across the PPE for both L and f_c. The space is split into two regions: A where κ is above the threshold, B where κ is below the threshold. In region A, three simulations do not show any substantial stratocumulus, with $L < 25$ g m^{-2} and $f_c < 0.5$. Four simulations show a very thin stratocumulus with $25 < L < 50$ g m^{-2} and initial $f_c > 0.7$. These clouds thicken slightly through the simulation

with L increasing up to 65 g m^{-2} and f_c decreasing by 0.1–0.2 as the cloud water aggregates. One point in this region, at coordinates $\Delta\theta = 5$ K and $\Delta q_t = -4$ g kg^{-1}, is better described alongside the simulations in region B and along the κ line. For those simulations, L begins in the range of 50–80 g m^{-2} and increases by 30–120 g m^{-2}. These clouds all have initial stratocumulus with $f_c > 0.9$ and most remain in that region or decrease to 0.8.

Low $\Delta\theta$ (a weak temperature inversion) generally produces low L, shown in Figure 3b, which reaches a minimum of 21 g m^{-2} at $\Delta\theta = 2.5$ K. With a stronger inversion L also generally increases, up to 160 g m^{-2} at $\Delta\theta = 20$ K. For high Δq_t (a moist free troposphere) L is high, up to 185 g m^{-2} for $\Delta q_t = 0$ g kg^{-1}. With a drier free troposphere L is generally lower, down to 20 g m^{-2} for $\Delta q_t = -8.7$ g kg^{-1}. The two parameters have a combined effect such that L is lowest for weak inversions with a dry free troposphere and highest for strong inversions with humidity similar to the boundary layer.

Low $\Delta\theta$ generally produces low f_c, shown in Figure 3d, down to 0.3 at $\Delta\theta = 2.5$ K. As the inversion gets stronger, f_c generally increases up to 0.9 at $\Delta\theta = 20$ K. At high Δq_t f_c approaches 1 for $\Delta q_t = 0$ g kg^{-1}. With a drier free troposphere f_c is generally lower, down to about 0.5 for $\Delta q_t = -8.7$ g kg^{-1}. As with L, the two parameters have a combined effect such that f_c is lowest for weak inversions with a dry free troposphere and highest for strong inversions with humidity similar to the boundary layer.

The spatial distribution of L is shown in Figure 4 at the end of each simulation for the 20-member PPE. Two of the simulations that do not form stratocumulus can be seen to the lower left of the figure as small cumulus clouds. Moving toward higher Δq_t and $\Delta\theta$ the plots show stratocumulus with higher L and f_c, and in the top row they become quite thick.

None of the simulations are drizzling significantly, but most region A simulations drizzle two to three orders of magnitude less than those in region B. The exception is the point at $\Delta\theta = 5$ K and $\Delta q_t = -4$ g kg^{-1} previously identified.

In summary, the PPE simulations show that cloud behavior across parameter space falls into two behavioral regimes that are approximately separated by the theoretical κ parameter threshold. Above the κ threshold, in region A, the simulations generally have very thin stratocumulus cloud or small cumulus that show little to no growth throughout the simulation. On and below the κ threshold, in region B, the simulations have stratocumulus cloud with a high f_c and a medium L that increases throughout the simulation. There is one point in region A at $\Delta\theta = 5$ K and $\Delta q_t = -4$ g kg^{-1} that behaves more like the simulations in region B.

4.3. Response Surface Analysis

Here we show emulator results from the 26-point training set. We used the PPE to train Gaussian process emulators of L, f_c, L tendency and f_c tendency. To validate the emulators, we compared the emulator predictions against model output from the validation runs. For all the emulators, the model values are within the emulator prediction 95% uncertainty ranges. The validation results can be found in Figure S1 in Supporting Information S1.

The L response surface in Figure 5a follows the behavior described previously by the training data, with low L for low Δq_t, low $\Delta\theta$ (dry, cool free troposphere) and high L for high Δq_t, high $\Delta\theta$ (moist, warm free troposphere). But the response surface reveals that Δq_t has the largest effect on L and for high Δq_t L becomes invariant to $\Delta\theta$. There is a local maximum at $\Delta\theta = 15$ K and $\Delta q_t = -4.5$ g kg^{-1}, which we will discuss in Section 5. The L tendency response surface in Figure 5b follows a similar pattern to L. The tendency is most positive where the L is high, that is, where there is most growth. The tendency is very close to zero where the liquid water path is low. It also shows a higher dependency on Δq_t and has a local maximum in a similar location. Additionally, the emulator predicts some slightly negative values in the corner of parameter space with low L, however the emulator has limited information at extremities so large uncertainties exist here.

The f_c response surface in Figure 5c also follows the behavior described previously, with low f_c for low Δq_t, low $\Delta\theta$ (dry, cool free troposphere) and high f_c for high Δq_t, high $\Delta\theta$ (moist, warm free troposphere). As with L, Δq_t has a larger effect than $\Delta\theta$, but it is not as stark as in L. The f_c tendency is mostly negative across the parameter space, with only a slightly positive region at low values of Δq_t and $\Delta\theta$. This is because there are only small cumulus clouds at start of the simulation (Figure 4) and these are mostly unchanging throughout the simulations, but increase in cloud cover slightly. Where f_c is approximately 1, f_c tendency is close to zero and slightly negative. The rest of the f_c tendency surface is very uneven (noisy) since there are only small changes in f_c throughout the
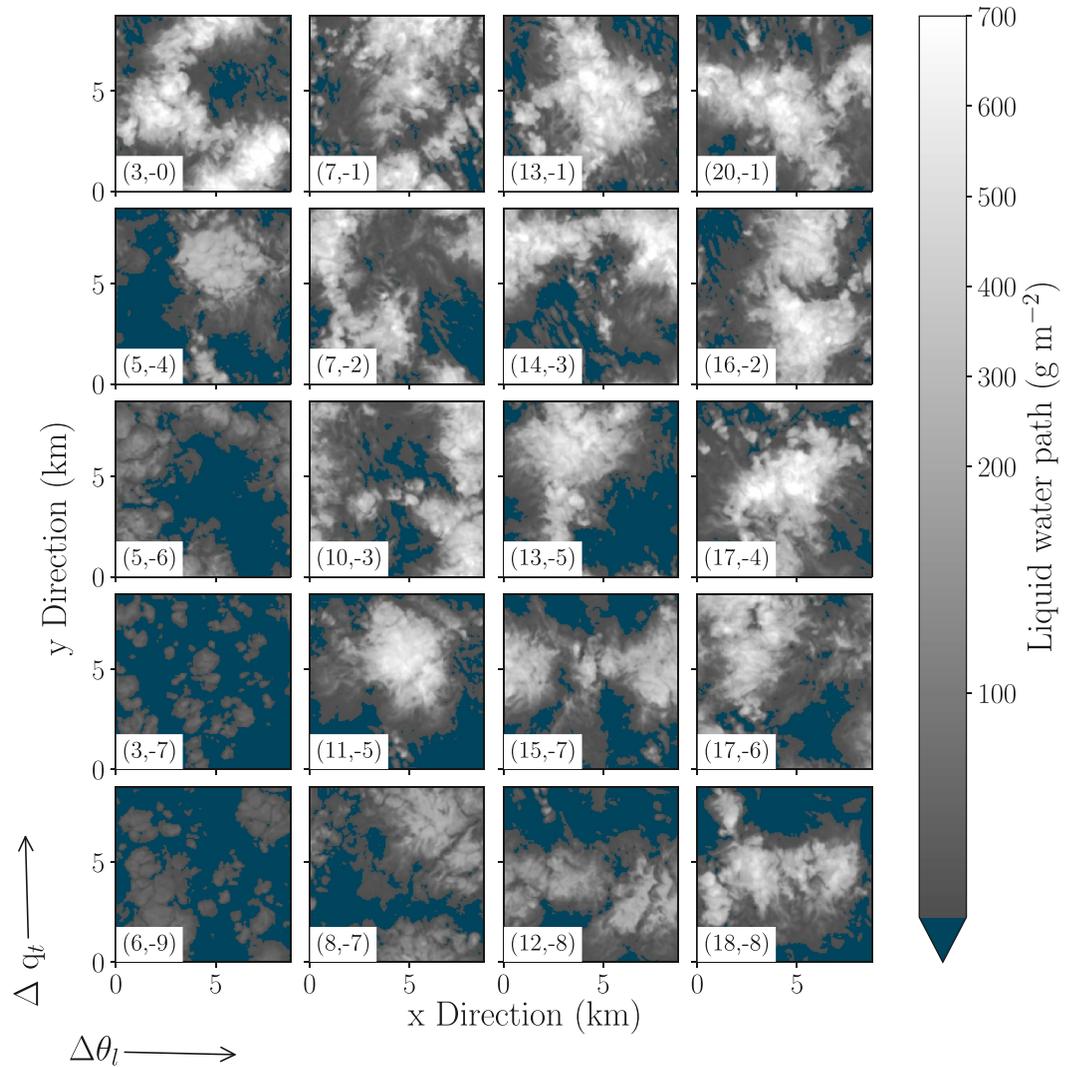
Figure 4. Liquid water path for the last timestep of the first 20 training simulations. Plots are ordered approximately by location in parameter space. The null value (dark blue) shows where liquid cloud droplet mass mixing ratio <0.01 g kg^{-1} at all levels.

simulations (Figure 3c). Some of the validation points are close in value to the predicted surface, but a few points are quite contrasting, which suggests that the surface is not very representative of the model behavior at these points.

The κ threshold separating regions A and B approximately follows the surface contours, except for f_c tendency. The surfaces show a smooth gradient between these regions of parameter space rather than a discontinuity. In the cloud behavior analysis in Section 4.2, there was a single point in region A at $\Delta\theta = 5$ K and $\Delta q_t = -4$ g kg^{-1} that did not fit with the other points in terms of behavior. We can now see in Figures 5a and 5b that the contours curve round in this part of parameter space.

5. Internal Variability

Clouds and cloud models contain many interacting nonlinear processes that make them sensitive to small variations in initial conditions. The output of two PPE members that are close together in parameter space may be quite different due to this internal variability, that is, only some portion of the difference is caused by perturbing the parameters. This variability creates a "bumpy" response surface because the output is affected by non-linearities in any direction from a single point on the surface, and the emulated function interpolates through each
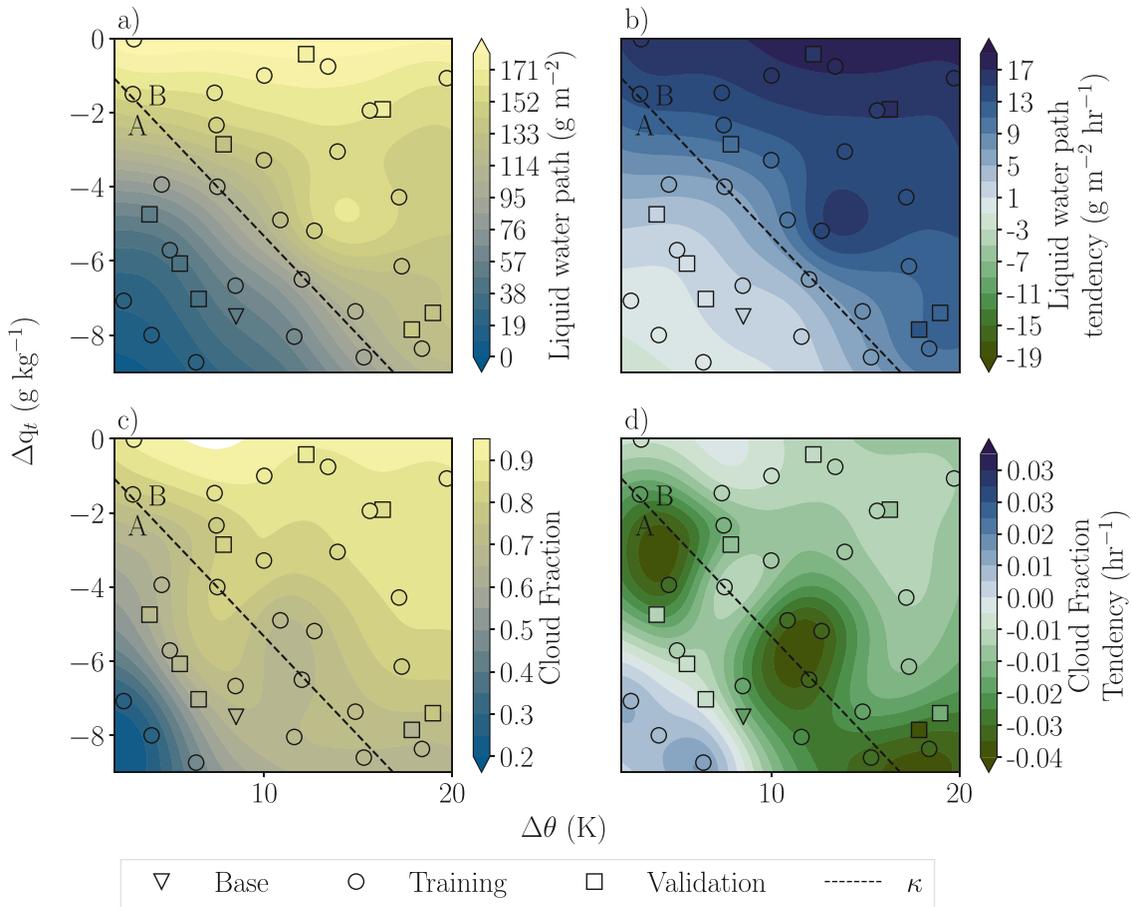
Figure 5. Response surfaces produced from emulator mean predictions. (a) Liquid water path, (b) liquid water path tendency, (c) cloud fraction and (d) cloud fraction tendency.

point exactly (see Figure 6a). In attempting to fit training data, the mean function may also distort in areas lacking data, creating additional extrema that are not based on the model's deterministic output. An example is the maximum around $\Delta\theta = 15$ and $\Delta q_t = -4.5$ in Figure 5a. These bumps and extrema do not allow the emulator to accurately represent the deterministic cloud behavior that we aim to capture with response surfaces.

We can quantify the internal variability affecting each model output by running "initial-condition" ensembles, where instead of perturbing cloud-controlling factors we slightly perturb the turbulence structure at the start of a simulation. Turbulence is initiated in MONC and other LES models by imposing small random temperature
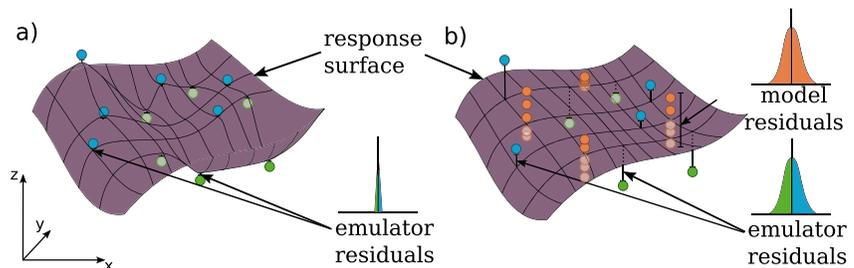
Figure 6. Schematic of the effect of adding a nugget term on the response surface smoothness. (a) The purple response surface interpolates exactly through the blue and green training points so the emulator residuals are zero. (b) The response surface is smooth after adding a nugget term, so the surface interpolates through a prescribed buffer around the blue and green training points. The nugget term is appropriately large when the distribution of model residuals matches the emulator residuals. Initial-condition ensembles have been run at a selection of points (orange) to gauge the nugget term.

fluctuations during simulation initialization. To make simulations repeatable, the randomization is usually seeded. However, by truly randomizing them, without changing the cloud-controlling factors, we can gauge how much fluctuation in the output is due to internal variability. Ideally, we could run initial-condition ensembles at every training point and build an emulator using the mean values at each point, but this is computationally expensive for many climate models. We therefore explore using a small number of initial-condition ensembles to estimate the variability and incorporate it into the emulator builds using a hyperparameter called a "nugget term." Instead of interpolating the training data exactly, it allows the mean function to pass within a buffer either side of the output value creating a much smoother response surface.

In the posterior Gaussian process, the covariance function estimates the uncertainty for any predicted point depending on its distance from the training data. In this study, the covariance between any two points is,

$$V(x_j, x_k) = \sigma^2 K(x_j, x_k),\tag{6}$$

where σ^2 is the variance of the Gaussian process and in this case $K(x_j, x_k)$ represents the Matérn class of covariance functions. The covariance function can be extended to include the nugget term, σ_N^2,

$$V(x_j, x_k) = \sigma^2 K(x_j, x_k) + \sigma_N^2 \delta_{j,k},\tag{7}$$

where $\delta_{j,k}$ is the Kronecker delta function, which equals 1 for $j = k$ and equals 0 otherwise. The nugget term is often included to alleviate numerical issues in deterministic models, but there are additional benefits to adding one (Andrianakis & Challenor, 2012; Gramacy & Lee, 2012). Practically, the nugget term is a variance that is added at each training point allowing the mean function to vary within that range and no longer interpolate exactly through that point.

For the response surface to most-realistically represent the model's deterministic behavior, we hypothesize that the variance added with the nugget term should be equal to the variance of the model's internal variability. In Figure 6a, the emulator mean function interpolates exactly through the training points resulting in a bumpy response surface, where the residuals between the emulator mean function (the response surface) and model outputs are zero. However, each training point is a single draw from the initial-condition ensemble (Figure 6b). With a nugget term that represents the variance of the initial-condition ensemble, the emulator residuals at training points vary around zero. Following our hypothesis, we aim to create a surface for which the distribution of emulator residuals at training points has a similar spread to the distribution of the initial-condition members, which represent the internal variability.

We ran 5-member ensembles at nine training points, which were selected to cover the parameter space well, with a particular focus on sampling the range of output values. The timeseries evolution of the ensembles is shown in Figure 3 and the intra-ensemble differences in the simulated final cloud fields are shown in Figure 7. Figure 8 shows that the variance increases with the mean value, which indicates the internal variability varies across parameter space. We make the assumption that the variance of one initial-condition ensemble is representative of the variance in nearby parameter space and can be applied to other training data in that area. The small sample size lowers the accuracy of the ensemble variances, however, we must approximate the variance because it is unfeasible to run larger ensembles at each point. There may be more appropriate methods to gauge the variance, for example, for some outputs it may be suitable to calculate the variance across the domain or timeseries.

We use the variance of the "model" residuals (difference between each ensemble member and the ensemble mean) to estimate an appropriate nugget term for the L emulator. For each of the training points, Z_i, in the training data set $Z_1, \ldots, Z_l$, running initial-condition ensembles gives a set of estimates, $\left(Z_i^{(1)}, \ldots, Z_i^{(k)}\right)$, for k ensemble members at Z_i. The ensemble means and residuals are calculated as

$$\overline{Z}_i = \frac{1}{k} \sum_{j=1}^{k} Z_i^{(j)}\tag{8}$$
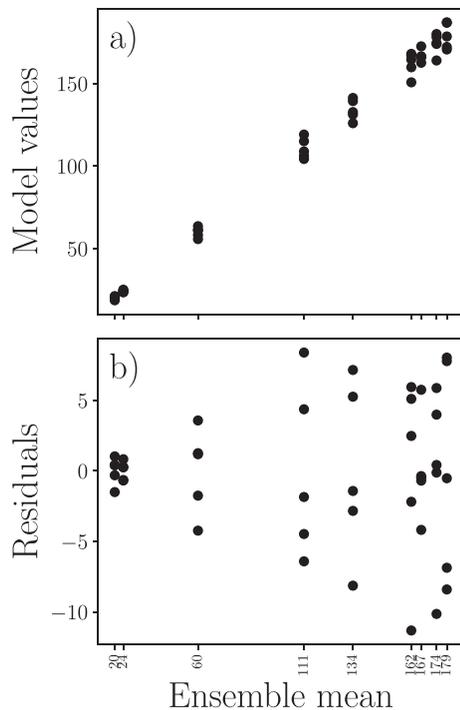
$$r_i^{(j)} = Z_i^{(j)} - \overline{Z}_i.\tag{9}$$
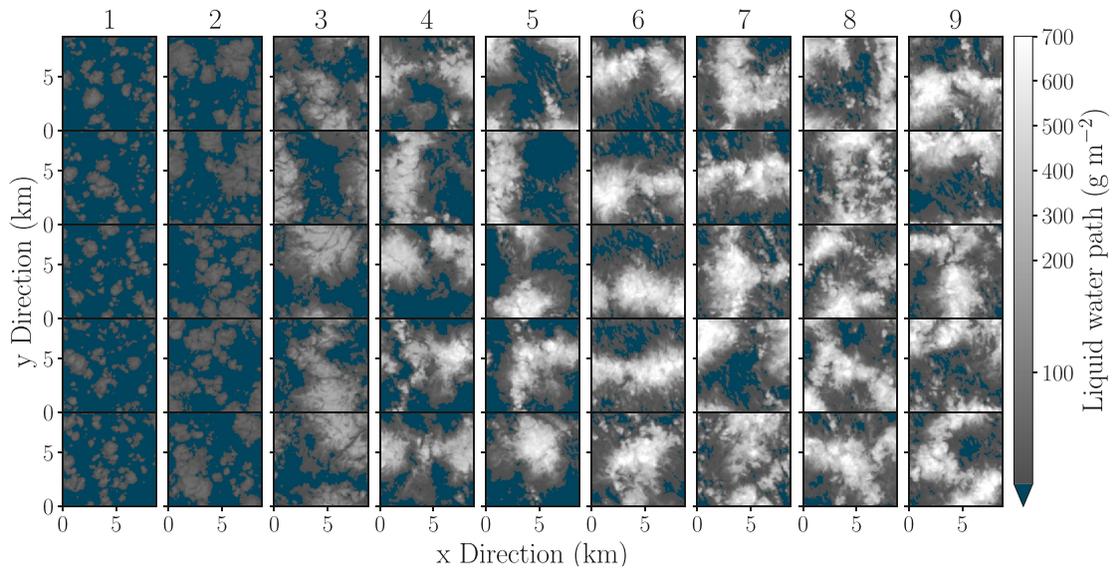
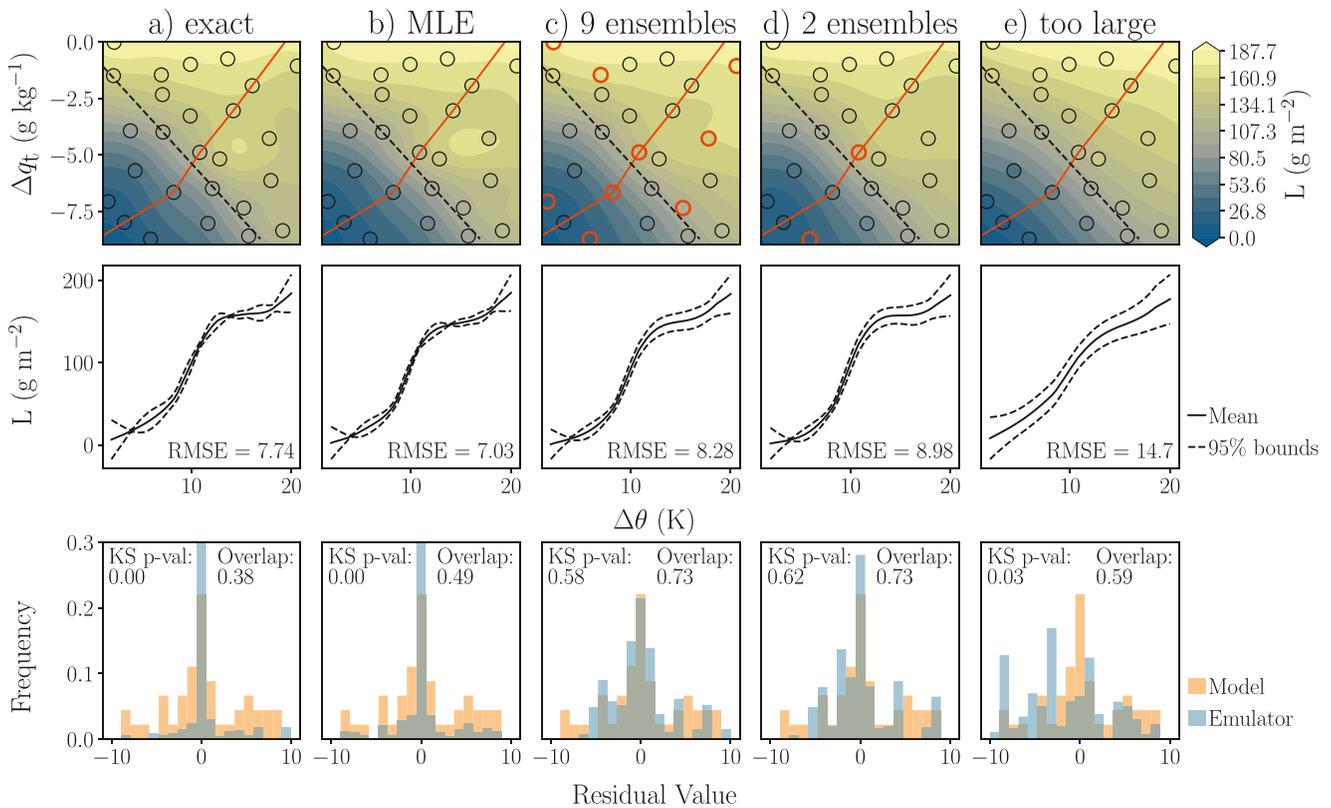**Figure 7.** In-cloud liquid water path in the final timestep for each five-member ensemble simulation.

The nugget term is applied as a vector, $V = (v_1, \ldots, v_l)$, where v_i is the variance of each ensemble, σ_i^2, that should be applied at each Z_i. We compared using all nine ensemble variances, applied to their nearest neighbors, against using just one ensemble variance for each regime. We used the Kolmogorov-Smirnov (KS) two-sample test to test whether these samples are statistically likely to be from the same distribution. For those with a *p*-value less than 0.05 we must reject the null hypothesis that the samples could be drawn from the same distribution.

For *L*, Figure 9 shows that just two ensemble points, one from each region, can be used to calculate the nugget vector and provides a similar result to using all nine ensembles. Without any nugget term applied, in Figure 9a, the response surface has an unfounded maxima. Using MLE to estimate the nugget term (Figure 9b) does not help to smooth the surface and does not make the two histograms comparable as the surface is still forced to pass too closely to the training output. We have shown the results for 9 (column c) and 2 (column d) ensemble points here. Most other combinations of points were sufficient, and many of the variances could be used as a single nugget term for all training points. The exceptions were the two ensemble points in the extremely low *L* corner of parameter space. If only these two were used, the nugget term was not sufficiently large. Figure 9e shows a nugget term that has been adjusted to be too large. Here, the response surface begins to default to the prior mean function and information about the relationship is lost, such as the lack of dependence on $\Delta\theta$ at low values.

Figure 10 shows the results using minimal ensemble points for the other emulators. For *L* tendency (column a) and f_c (column b), 2 ensemble points were sufficient, but it produced a better result for f_c when the parameter space was split at the steeper gradient, with 1 point for the 3 values in the low f_c corner and 1 point for the rest. There is not much visible smoothing in the response surface suggesting that an ensemble member with larger variance in region B might give a better result. For the f_c tendency, at least 5 ensemble points were required for an appropriate nugget term. In this case, the variance in the output is quite changeable across parameter space so more sampling is required than for the other outputs. For response surfaces with the nugget term

Figure 8. Initial-condition ensemble variance. (a) The 5-member ensemble model values and (b) the residual values against the nine ensemble mean values.

Figure 9. The mean liquid water path emulator with nugget terms applied. (a) No nugget term, (b) maximum likelihood estimation, (c) 9 ensemble points (d) 2 ensemble points, and (e) a term that is only just too large. Top row: emulator predicted response surfaces with transect line. Orange circles indicate which ensemble points were used in the nugget term calculation. Middle row: transects along orange line showing mean emulator function and associated uncertainty. Bottom row: histogram comparison of emulator and model residuals (Figure 6). The RMSE, Kolmogorov-Smirnov *p*-values, and overlap fractions are given for each nugget term.

added, the behavior across parameter space remains approximately as described in Section 4.2, but it is smoother and represents the model's general behavior better. Figure S2 in Supporting Information S1 shows the validation results of these response surfaces.

This analysis shows that smoother, more deterministic response surfaces can be produced by estimating the internal variability from initial-condition ensembles. If the internal variability is sampled in areas that capture the range of output behavior, or over distinct regimes, fewer points are needed. For smoothly varying output, just one initial-condition ensemble may suffice. With more regions of differing behavior and a less well-behaved (more noisy) surface then neither 2 nor 5 ensemble members is likely to be enough.

6. Discussion and Conclusions

We have used Gaussian process emulation to analyze and visualize the dependence of stratocumulus clouds on the initial profiles of two cloud-controlling factors with a relatively small computational cost.

We found there are two distinct behavioral cloud regimes in the explored parameter space, with a smooth transition between them. Our findings agree with Mellado (2017), in that cloud-top entrainment instability is not strong enough to break up the cloud by itself, and there is no distinct point beyond which the cloud rapidly breaks up, as hypothesized by Lilly (1968), Randall (1980) and Deardorff (1980). However the κ parameter does approximately mark a behavior change between region A (Figure 5), which has thin stratocumulus cloud (or small cumulus) and very little growth, and region B, which has stratocumulus that starts with high cloud fraction, moderate liquid water path, and grows throughout the simulation.

Internal variability presents a challenge for training an emulator that describes the deterministic response of cloud fields to cloud-controlling factors. Failure to account for variability resulted in bumpy response surfaces.
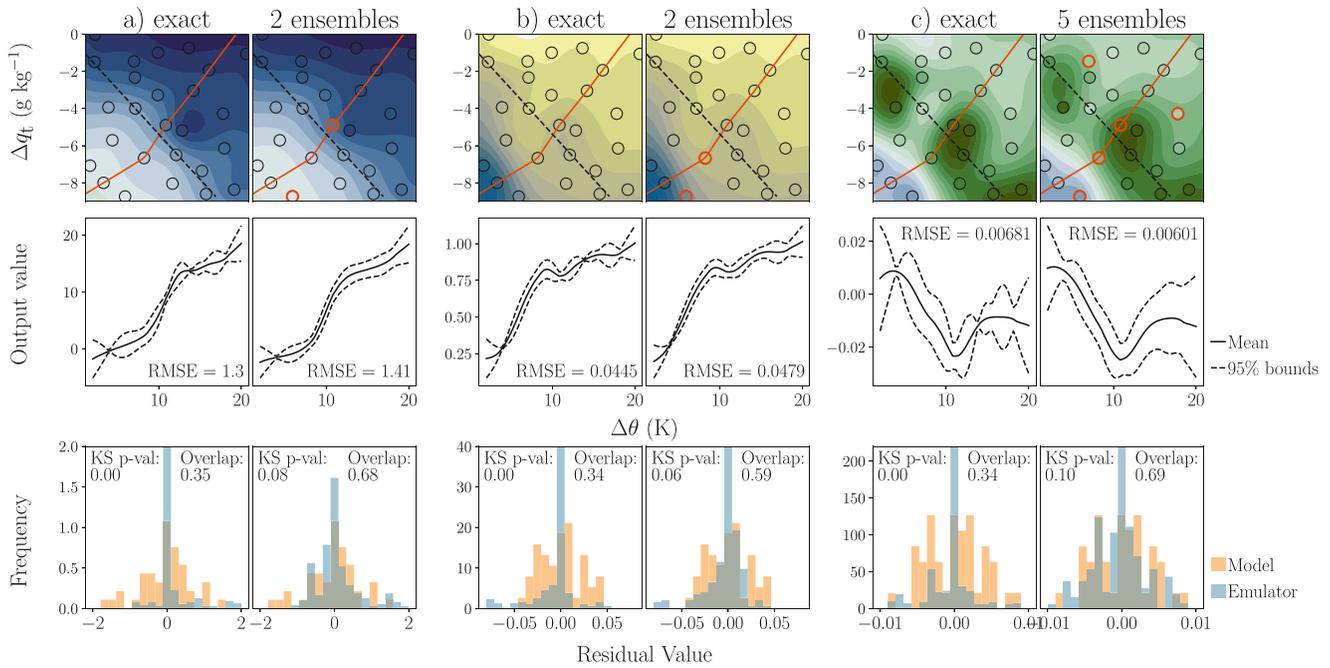
Figure 10. Cloud property emulators with and without nugget terms applied. (a) Liquid water path tendency, (b) cloud fraction and (c) cloud fraction tendency. Top row: emulator predicted response surfaces. Orange circles indicate which ensemble points were used in the nugget term calculation. Middle row: transects along the orange line in top row showing mean emulator function and the associated uncertainty. Bottom row: histogram comparison of emulator and model residuals (Figure 6). The RMSE, Kolmogorov-Smirnov p-values, and overlap fractions are given for each nugget term.

Although previous studies have used initial-condition-ensemble means as training data at each point (Johnson et al., 2011) this is not feasible with cloud or climate models. Our approach showed that sampling the internal variability in each distinct regime was usually sufficient to approximate the size of the nugget term. However, for more variable output more initial-condition ensembles are likely necessary to capture how the variance changes across the parameter space. Additionally, sometimes the small ensemble number will not give an accurate variance at a training point. For the f_c emulators, there was one ensemble point that had a much smaller variance and thus did not produce a large enough nugget term when used with all 9 members. This method is dependent on the training data and the chosen ensembles, and may require some adjustment of the nugget term on inspecting the emulator. Assessing the emulator performance, the detail in the response surface (whether it could be physical or not), the validation result, as well as the error bars are all part of checking whether a nugget term is appropriate.

Without including aerosol processes in the simulation some cloud breakup mechanisms are not accounted for in our simulations, such as rain-depletion feedbacks (Goren et al., 2019). We also used a lower fixed droplet number concentration than Stevens et al. (2005), however we repeated the simulations with a higher fixed concentration and found the general behaviors in each region aligned with the lower concentration case shown here. The lack of rapid cloud breakup fits with the conclusion in Mellado (2017) that the feedback mechanism is too weak to break up the cloud by itself.

One unexpected benefit of producing a response surface from a PPE and emulator was the ability to identify outliers in the data. Against the backdrop of the PPE and the emulated surface these simulations clearly stand out, allowing further investigation into why they do not fit with the rest of the data. In some cases, this could identify an interesting region of parameter space in the real world, or an internal variability extremity that could be investigated with a small ensemble, or perhaps a collection of parameter settings for which the model is unstable. Otherwise, it may simply be a corrupted value in the model and can be discarded. Another benefit of emulation is the ability to constrain the output using history matching, a method where emulator predictions are compared with observations, which has been used to constrain aerosol forcings (Johnson et al., 2018; Regayre et al., 2020, 2023; Watson-Parris et al., 2020). Implausible regions of parameter space can be "ruled out" using reanalysis-derived values of the input parameters and satellite retrievals of the outputs, allowing for emulator uncertainty, observational uncertainty and model structural errors.

As climate models get more complex, machine learning is an invaluable tool for understanding processes. The number of simulations required to fully explore uncertainties and certain aspects of models is already infeasible, particularly with the nonlinear behavior of clouds. Statistical emulation has already proven to be immensely useful for sensitivity analysis of model parameters in climate studies. Here we have shown it in a different capacity by perturbing cloud-controlling factors, which has only recently begun to be explored. We believe this is a unique method for exploring cloud processes, and it can be expanded to include changes in aerosol concentrations, parameterization coefficients and more meteorological parameters.

Data Availability Statement

The PPE data from the MONC model can be found on Zenodo at https://doi.org/10.5281/zenodo.10036710 (Sansom, 2023). All code used in the analysis can be found on GitHub, licensed under MIT, at https://github.com/eers1/dycoms_analysis, with version 1 archived on Zenodo at https://doi.org/10.5281/zenodo.11204877 (Sansom, 2024). All analysis was done using Python which is Open Source. A version of the MONC model is also available on GitHub at https://github.com/Leeds-MONC.

References

Ackerman, A. S., van Zanten, M. C., Stevens, B., Savic-Jovcic, V., Bretherton, C. S., Chlond, A., et al. (2009). Large-eddy simulations of a drizzling, stratocumulus-topped marine boundary layer. *Monthly Weather Review*, *137*(3), 1083–1110. https://doi.org/10.1175/2008MWR2582.1

Andrianakis, I., & Challenor, P. G. (2012). The effect of the nugget on Gaussian process emulators of computer models. *Computational Statistics & Data Analysis*, *56*(12), 4215–4228. https://doi.org/10.1016/j.csda.2012.04.020

Bellon, G., & Stevens, B. (2013). Time scales of the trade wind boundary layer adjustment. *Journal of the Atmospheric Sciences*, *70*(4), 1071–1083. https://doi.org/10.1175/JAS-D-12-0219.1

Bellouin, N., Quaas, J., Gryspeerdt, E., Kinne, S., Stier, P., Watson-Parris, D., et al. (2020). Bounding global aerosol radiative forcing of climate change. *Blackwell Publishing Ltd*, *58*(1). https://doi.org/10.1029/2019RG000660

Blossey, P. N., Bretherton, C. S., Cheng, A., Endo, S., Heus, T., Lock, A. P., & van der Dussen, J. J. (2016). CGILS Phase 2 LES intercomparison of response of subtropical marine low cloud regimes to CO2 quadrupling and a CMIP3 composite forcing change. *Journal of Advances in Modeling Earth Systems*, *8*(4), 1714–1726. https://doi.org/10.1002/2016MS000765

Bony, S., & Dufresne, J.-L. (2005). Marine boundary layer clouds at the heart of tropical cloud feedback uncertainties in climate models. *Geophysical Research Letters*, *32*(20). https://doi.org/10.1029/2005GL023851

Bretherton, C. S. (2015). Insights into low-latitude cloud feedbacks from high-resolution models. *Philosophical Transactions of the Royal Society A: Mathematical, Physical & Engineering Sciences*, *373*(2054), 20140415. https://doi.org/10.1098/rsta.2014.0415

Brown, A. R., Derbyshire, S. H., & Mason, P. J. (1994). Large-eddy simulation of stable atmospheric boundary layers with a revised stochastic subgrid model. *Quarterly Journal of the Royal Meteorological Society*, *120*(520), 1485–1512. https://doi.org/10.1002/qj.49712052004

Brown, N., Weiland, M., Hill, A., Shipway, B., Allen, T., Maynard, C., & Rezny, M. (2020). A highly scalable met office NERC cloud model. https://doi.org/10.48550/arXiv.2009.12849

Ceppi, P., Brient, F., Zelinka, M. D., & Hartmann, D. L. (2017). Cloud feedback mechanisms and their representation in global climate models. *Wiley Interdisciplinary Reviews: Climate Change*, *8*(4), e465. https://doi.org/10.1002/wcc.465

Dal Gesso, S., Van Der Dussen, J. J., Siebesma, A. P., De Roode, S. R., Boutle, I. A., Kamae, Y., et al. (2015). A single-column model inter-comparison on the stratocumulus representation in present-day and future climate. *Journal of Advances in Modeling Earth Systems*, *7*(2), 617–647. https://doi.org/10.1002/2014MS000377

Dearden, C., Hill, A., Coe, H., & Choularton, T. (2018). The role of droplet sedimentation in the evolution of low-level clouds over southern West Africa. *Atmospheric Chemistry and Physics*, *18*(19), 14253–14269. https://doi.org/10.5194/acp-18-14253-2018

Deardorff, J. W. (1980). Cloud top entrainment instability. *Journal of the Atmospheric Sciences*, *37*(1), 131–147. https://doi.org/10.1175/1520-0469(1980)037⟨0131:CTEI⟩2.0.CO;2

Douglas, A., & L'Ecuyer, T. (2020). Quantifying cloud adjustments and the radiative forcing due to aerosol-cloud interactions in satellite observations of warm marine clouds. *Atmospheric Chemistry and Physics*, *20*(10), 6225–6241. https://doi.org/10.5194/acp-20-6225-2020

Dufresne, J. L., & Bony, S. (2008). An assessment of the primary sources of spread of global warming estimates from coupled atmosphere-ocean models. *Journal of Climate*, *21*(19), 5135–5144. https://doi.org/10.1175/2008JCLI2239.1

Feingold, G., McComiskey, A., Yamaguchi, T., Johnson, J. S., Carslaw, K. S., & Schmidte, K. S. (2016). New approaches to quantifying aerosol influence on the cloud radiative effect. *Proceedings of the National Academy of Sciences of the United States of America*, *113*(21), 5812–5819. https://doi.org/10.1073/pnas.1514035112

Field, P. R., Hill, A., Shipway, B., Furtado, K., Wilkinson, J., Miltenberger, A., et al. (2023). Implementation of a double moment cloud microphysics scheme in the UK met office regional numerical weather prediction model. *Quarterly Journal of the Royal Meteorological Society*, *149*(752), 703–739. https://doi.org/10.1002/qj.4414

Fletcher, R. (1987). *Practical methods of optimization* (2nd ed.). Wiley.

Ghonima, M. S., Norris, J. R., Heus, T., & Kleissl, J. (2015). Reconciling and validating the cloud thickness and liquid water path tendencies proposed by R. Wood and J. J. van der Dussen et al. *Journal of the Atmospheric Sciences*, *72*(5), 2033–2040. https://doi.org/10.1175/JAS-D-14-0287.1

Glassmeier, F., Hoffmann, F., Johnson, J. S., Yamaguchi, T., Carslaw, K. S., & Feingold, G. (2019). An emulator approach to stratocumulus susceptibility. *Atmospheric Chemistry and Physics*, *19*(15), 10191–10203. https://doi.org/10.5194/acp-19-10191-2019

Goren, T., Kazil, J., Hoffmann, F., Yamaguchi, T., & Feingold, G. (2019). Anthropogenic air pollution delays marine stratocumulus breakup to open cells. *Geophysical Research Letters*, *46*(23), 14135–14144. https://doi.org/10.1029/2019GL085412

Gramacy, R. B., & Lee, H. K. (2012). Cases for the nugget in modeling computer experiments. *Statistics and Computing*, *22*(3), 713–722. https://doi.org/10.1007/s11222-010-9224-x

Gray, M. E. B., Petch, J., Derbyshire, S. H., Brown, A. R., Lock, A. P., Swann, H. A., & Brown, P. R. A. (2001). Version 2.3 of the met office large eddy model: Part II. Scientific documentation. *Met O (APR) Turbulence and Diffusion Note No. 276.*

Hartmann, D. L., Ockert-Bell, M. E., & Michelsen, M. L. (1992). The effect of cloud type on Earth's energy balance: Global analysis. *Journal of Climate*, *5*(11), 1281–1304. https://doi.org/10.1175/1520-0442(1992)005⟨1281:teocto⟩2.0.co;2

Henderson, D. A., Boys, R. J., Krishnan, K. J., Lawless, C., & Wilkinson, D. J. (2009). Bayesian emulation and calibration of a stochastic computer model of mitochondrial DNA deletions in substantia Nigra Neurons. *Journal of the American Statistical Association*, *104*(485), 76–87. https://doi.org/10.1198/jasa.2009.0005

Hill, A. A., Shipway, B. J., & Boutle, I. A. (2015). How sensitive are aerosol-precipitation interactions to the warm rain representation? *Journal of Advances in Modeling Earth Systems*, *7*(3), 987–1004. https://doi.org/10.1002/2014MS000422

Hoffmann, F., Glassmeier, F., Yamaguchi, T., & Feingold, G. (2020). Liquid water path steady states in stratocumulus: Insights from process-level emulation and mixed-layer theory. *Journal of the Atmospheric Sciences*, *77*(6), 2203–2215. https://doi.org/10.1175/jas-d-19-0241.1

Igel, A. L., van den Heever, S. C., & Johnson, J. S. (2018). Meteorological and land surface properties impacting sea breeze extent and aerosol distribution in a dry environment. *Journal of Geophysical Research: Atmospheres*, *123*(1), 22–37. https://doi.org/10.1002/2017JD027339

Johnson, J. S., Cui, Z., Lee, L. A., Gosling, J. P., Blyth, A. M., & Carslaw, K. S. (2015). Evaluating uncertainty in convective cloud microphysics using statistical emulation. *Journal of Advances in Modeling Earth Systems*, *7*(1), 162–187. https://doi.org/10.1002/2014MS000383

Johnson, J. S., Gosling, J. P., & Kennedy, M. C. (2011). Gaussian process emulation for second-order Monte Carlo simulations. *Journal of Statistical Planning and Inference*, *141*(5), 1838–1848. https://doi.org/10.1016/j.jspi.2010.11.034

Johnson, J. S., Regayre, L. A., Yoshioka, M., Pringle, K. J., Lee, L. A., Sexton, D. M., et al. (2018). The importance of comprehensive parameter sampling and multiple observations for robust constraint of aerosol radiative forcing. *Atmospheric Chemistry and Physics*, *18*(17), 13031–13053. https://doi.org/10.5194/acp-18-13031-2018

Khairoutdinov, M., & Kogan, Y. (2000). A new cloud physics parameterization in a large-eddy simulation model of marine stratocumulus. *Monthly Weather Review*, *128*(1), 229–243. https://doi.org/10.1175/1520-0493(2000)128⟨0229:ANCPPI⟩2.0.CO;2

Kuo, H.-C., & Schubert, W. H. (1988). Stability of cloud-topped boundary layers. *Quarterly Journal of the Royal Meteorological Society*, *114*(482), 887–916. https://doi.org/10.1002/qj.49711448204

Lawrence, B. N., Bennett, V. L., Churchill, J., Juckes, M., Kershaw, P., Pascoe, S., et al. (2013). Storing and manipulating environmental big data with JASMIN. In *2013 IEEE international conference on big data* (pp. 68–75). https://doi.org/10.1109/BigData.2013.6691556

Lee, L. A., Carslaw, K. S., Pringle, K. J., Mann, G. W., & Spracklen, D. V. (2011). Emulation of a complex global aerosol model to quantify sensitivity to uncertain parameters. *Atmospheric Chemistry and Physics*, *11*(23), 12253–12273. https://doi.org/10.5194/acp-11-12253-2011

Lee, L. A., Pringle, K. J., Reddington, C. L., Mann, G. W., Stier, P., Spracklen, D. V., et al. (2013). The magnitude and causes of uncertainty in global model simulations of cloud condensation nuclei. *Atmospheric Chemistry and Physics*, *13*(17), 8879–8914. https://doi.org/10.5194/acp-13-8879-2013

Lilly, D. K. (1968). Models of cloud-topped mixed layers under a strong inversion. *Quarterly Journal of the Royal Meteorological Society*, *94*(401), 292–309. https://doi.org/10.1002/qj.49709440106

Loeppky, J. L., Sacks, J., & Welch, W. J. (2009). Choosing the sample size of a computer experiment: A practical guide. *Technometrics*, *51*(4), 366–376. https://doi.org/10.1198/TECH.2009.08040

Lund, M. T., Myhre, G., & Samset, B. H. (2019). Anthropogenic aerosol forcing under the shared socioeconomic pathways. *Atmospheric Chemistry and Physics*, *19*(22), 13827–13839. https://doi.org/10.5194/ACP-19-13827-2019

MacVean, M. K., & Mason, P. J. (1990). Cloud-top entrainment instability through small-scale mixing and its parameterization in numerical models. *Journal of the Atmospheric Sciences*, *47*(8), 1012–1030. https://doi.org/10.1175/1520-0469(1990)047⟨1012:CTEITS⟩2.0.CO;2

Malavelle, F. F., Haywood, J. M., Jones, A., Gettelman, A., Clarisse, L., Bauduin, S., et al. (2017). Strong constraints on aerosol-cloud interactions from volcanic eruptions. *Nature*, *546*(7659), 485–491. https://doi.org/10.1038/nature22974

Marshall, L. R., Johnson, J. S., Mann, G. W., Lee, L., Dhomse, S. S., Regayre, L., et al. (2019). Exploring how eruption source parameters affect volcanic radiative forcing using statistical emulation. *Journal of Geophysical Research: Atmospheres*, *124*(2), 964–985. https://doi.org/10.1029/2018JD028675

Marshall, L. R., Schmidt, A., Johnson, J. S., Mann, G. W., Lee, L. A., Rigby, R., & Carslaw, K. S. (2021). Unknown eruption source parameters cause large uncertainty in historical volcanic radiative forcing reconstructions. *Journal of Geophysical Research: Atmospheres*, *126*(13), e2020JD033578. https://doi.org/10.1029/2020JD033578

Mellado, J. P. (2017). Cloud-top entrainment in stratocumulus clouds. *Annual Review of Fluid Mechanics*, *49*(1), 145–169. https://doi.org/10.1146/annurev-fluid-010816-060231

Morris, M. D., & Mitchell, T. J. (1995). Exploratory designs for computational experiments. *Journal of Statistical Planning and Inference*, *43*(3), 381–402. https://doi.org/10.1016/0378-3758(94)00035-T

Myhre, G., Shindell, D., Bréon, F.-M., Collins, W., Fuglestvedt, J., Huang, J., et al. (2013). Anthropogenic and natural radiative forcing. In *Climate Change 2013: The physical science basis. Contribution of working Group I to the fifth assessment report of the intergovernmental panel on climate change (Tech. Rep.)*. Cambridge University Press. https://doi.org/10.1017/CBO9781107415324

Nuijens, L., & Siebesma, A. P. (2019). Boundary layer clouds and convection over subtropical oceans in our current and in a warmer climate. *Current Climate Change Reports*, *5*(2), 80–94. https://doi.org/10.1007/S40641-019-00126-X

O'Hagan, A. (2006). Bayesian analysis of computer code outputs: A tutorial. *Reliability Engineering & System Safety*, *91*(10–11), 1290–1300. https://doi.org/10.1016/j.ress.2005.11.025

Oyebamiji, O. K., Wilkinson, D. J., Jayathilake, P. G., Curtis, T. P., Rushton, S. P., Li, B., & Gupta, P. (2017). Gaussian process emulation of an individual-based model simulation of microbial communities. *Journal of Computational Science*, *22*, 69–84. https://doi.org/10.1016/j.jocs.2017.08.006

Park, J. M., van den Heever, S. C., Igel, A. L., Grant, L. D., Johnson, J. S., Saleeby, S. M., et al. (2020). Environmental controls on tropical sea breeze convection and resulting aerosol redistribution. *Journal of Geophysical Research: Atmospheres*, *125*(6). https://doi.org/10.1029/2019JD031699

Park, J.-S., & Baek, J. (2001). Efficient computation of maximum likelihood estimators in a spatial linear model with power exponential covariogram. *Computers & Geosciences*, *27*(1), 1–7. https://doi.org/10.1016/S0098-3004(00)00016-9

Peace, A. H., Carslaw, K. S., Lee, L. A., Regayre, L. A., Booth, B. B., Johnson, J. S., & Bernie, D. (2020). Effect of aerosol radiative forcing uncertainty on projected exceedance year of a 1.5°C global temperature rise. *Environmental Research Letters*, *15*(9), 0940a6. https://doi.org/10.1088/1748-9326/ABA20C

Pope, C. A., Gosling, J. P., Barber, S., Johnson, J. S., Yamaguchi, T., Feingold, G., & Blackwell, P. G. (2021). Gaussian process modeling of heterogeneity and discontinuities using Voronoi tessellations. *Technometrics*, *63*(1), 53–63. https://doi.org/10.1080/00401706.2019.1692696

Pressel, K. G., Mishra, S., Schneider, T., Kaul, C. M., & Tan, Z. (2017). Numerics and subgrid-scale modeling in large eddy simulations of stratocumulus clouds. *Journal of Advances in Modeling Earth Systems*, *9*(2), 1342–1365. https://doi.org/10.1002/2016MS000778

Randall, D. A. (1980). Conditional instability of the first kind up-side down. *Journal of the Atmospheric Sciences*, *37*(1), 125–130. https://doi.org/10.1175/1520-0469(1980)037⟨0125:CIOTFK⟩2.0.CO;2

Rasmussen, C. E., & Williams, C. K. I. (2006). *Gaussian processes for machine learning*. The MIT Press.

R Core Team. (2018). *R: A language and environment for statistical computing*. R Foundation for Statistical Computing.

Regayre, L. A., Deaconu, L., Grosvenor, D. P., Sexton, D. M. H., Symonds, C., Langton, T., et al. (2023). Identifying climate model structural inconsistencies allows for tight constraint of aerosol radiative forcing. *Atmospheric Chemistry and Physics*, *23*(15), 8749–8768. https://doi.org/10.5194/acp-23-8749-2023

Regayre, L. A., Johnson, J. S., Yoshioka, M., Pringle, K. J., Sexton, D. M., Booth, B. B., et al. (2018). Aerosol and physical atmosphere model parameters are both important sources of uncertainty in aerosol ERF. *Atmospheric Chemistry and Physics*, *18*(13), 9975–10006. https://doi.org/10.5194/acp-18-9975-2018

Regayre, L. A., Pringle, K. J., Booth, B. B., Lee, L. A., Mann, G. W., Browse, J., et al. (2014). Uncertainty in the magnitude of aerosol-cloud radiative forcing over recent decades. *Geophysical Research Letters*, *41*(24), 9040–9049. https://doi.org/10.1002/2014GL062029

Regayre, L. A., Pringle, K. J., Lee, L. A., Rap, A., Browse, J., Mann, G. W., et al. (2015). The climatic importance of uncertainties in regional aerosol-cloud radiative forcings over recent decades. *Journal of Climate*, *28*(17), 6589–6607. https://doi.org/10.1175/JCLI-D-15-0127.1

Regayre, L. A., Schmale, J., Johnson, J. S., Tatzelt, C., Baccarini, A., Henning, S., et al. (2020). The value of remote marine aerosol measurements for constraining radiative forcing uncertainty. *Atmospheric Chemistry and Physics*, *20*(16), 10063–10072. https://doi.org/10.5194/acp-20-10063-2020

Roustant, O., Ginsbourger, D., & Deville, Y. (2012). DiceKriging, DiceOptim: Two R packages for the analysis of computer experiments by Kriging-based metamodeling and optimization. *Journal of Statistical Software*, *51*(1), 1–55. https://doi.org/10.18637/jss.v051.i01

Saltelli, A., Chan, K., & Scott, E. M. (2000). *Sensitivity analysis*. Wiley.

Sansom, R. W. N. (2023). An LES perturbed parameter ensemble of free-tropospheric cloud-controlling factors on stratocumulus [Dataset]. *Zenodo*. https://doi.org/10.5281/zenodo.10036710

Sansom, R. W. N. (2024). eers1/dycoms_analysis: Initial release (Version v1) [Software]. *Zenodo*. https://doi.org/10.5281/zenodo.11204877

Schneider, T., Kaul, C. M., & Pressel, K. G. (2019). Possible climate transitions from breakup of stratocumulus decks under greenhouse warming. *Nature Geoscience*, *12*(3), 164–168. https://doi.org/10.1038/s41561-019-0310-1

Seinfeld, J. H., Bretherton, C., Carslaw, K. S., Coe, H., DeMott, P. J., Dunlea, E. J., et al. (2016). Improving our fundamental understanding of the role of aerosol-cloud interactions in the climate system. *Proceedings of the National Academy of Sciences of the United States of America*, *113*(21), 5781–5790. https://doi.org/10.1073/PNAS.1514043113/SUPPL{_}FILE/PNAS.201514043SI.PDF

Shen, Z., Sridhar, A., Tan, Z., Jaruga, A., & Schneider, T. (2022). A library of large-eddy simulations forced by global climate models. *Journal of Advances in Modeling Earth Systems*, *14*(3), e2021MS002631. https://doi.org/10.1029/2021MS002631

Shipway, B. J., & Hill, A. A. (2012). Diagnosis of systematic differences between multiple parametrizations of warm rain microphysics using a kinematic framework. *Quarterly Journal of the Royal Meteorological Society*, *138*(669), 2196–2211. https://doi.org/10.1002/qj.1913

Siems, S. T., Bretherton, C. S., Baker, M. B., Shy, S., & Breidenthal, R. E. (1990). Buoyancy reversal and cloud-top entrainment instability. *Quarterly Journal of the Royal Meteorological Society*, *116*(493), 705–739. https://doi.org/10.1002/qj.49711649309

Smith, C. J., Kramer, R., Myhre, G., Alterskjr, K., Collins, W., Sima, A., et al. (2020). Effective radiative forcing and adjustments in CMIP6 models. *Atmospheric Chemistry and Physics*, *20*(16), 9591–9618. https://doi.org/10.5194/acp-20-9591-2020

Stechmann, S. N., & Hottovy, S. (2016). Cloud regimes as phase transitions. *Geophysical Research Letters*, *43*(12), 6579–6587. https://doi.org/10.1002/2016GL069396

Stevens, B., & Feingold, G. (2009). Untangling aerosol effects on clouds and precipitation in a buffered system. *Nature Publishing Group*, *461*(7264), 607–613. https://doi.org/10.1038/nature08281

Stevens, B., Lenschow, D. H., Faloona, I., Moeng, C.-H., Lilly, D. K., Blomquist, B., et al. (2003). On entrainment rates in nocturnal marine stratocumulus. *Quarterly Journal of the Royal Meteorological Society*, *129*(595), 3469–3493. https://doi.org/10.1256/qj.02.202

Stevens, B., Moeng, C. H., Ackerman, A. S., Bretherton, C. S., Chlond, A., de Roode, S., et al. (2005). Evaluation of large-eddy simulations via observations of nocturnal marine stratocumulus. *Monthly Weather Review*, *133*(6), 1443–1462. https://doi.org/10.1175/MWR2930.1

Van Der Dussen, J. J., De Roode, S. R., & Siebesma, A. P. (2014). Factors controlling rapid stratocumulus cloud thinning. *Journal of the Atmospheric Sciences*, *71*(2), 655–664. https://doi.org/10.1175/JAS-D-13-0114.1

Watson-Parris, D., Bellouin, N., Deaconu, L. T., Schutgens, N. A. J., Yoshioka, M., Regayre, L. A., et al. (2020). Constraining uncertainty in aerosol direct forcing. *Geophysical Research Letters*, *47*(9), e2020GL087141. https://doi.org/10.1029/2020GL087141

Wellmann, C., Barrett, A. I., Johnson, J. S., Kunz, M., Vogel, B., Carslaw, K. S., & Hoose, C. (2018). Using emulators to understand the sensitivity of deep convective clouds and hail to environmental conditions. *Journal of Advances in Modeling Earth Systems*, *10*(12), 3103–3122. https://doi.org/10.1029/2018MS001465

Wellmann, C., I Barrett, A., S Johnson, J., Kunz, M., Vogel, B., S Carslaw, K., & Hoose, C. (2020). Comparing the impact of environmental conditions and microphysics on the forecast uncertainty of deep convective clouds and hail. *Atmospheric Chemistry and Physics*, *20*(4), 2201–2219. https://doi.org/10.5194/acp-20-2201-2020

Williamson, D., & Blaker, A. T. (2014). Evolving Bayesian emulators for structured Chaotic time series, with application to large climate models. *SIAM/ASA Journal on Uncertainty Quantification*, *2*(1), 1–28. https://doi.org/10.1137/120900915

Wood, R. (2012). Stratocumulus clouds. *Monthly Weather Review*, *140*(8), 2373–2423. https://doi.org/10.1175/MWR-D-11-00121.1

Xiao, H., Wu, C. M., & Mechoso, C. R. (2011). Buoyancy reversal, decoupling and the transition from stratocumulus to shallow cumulus topped marine boundary layers. *Climate Dynamics*, *37*(5), 971–984. https://doi.org/10.1007/s00382-010-0882-3

Yamaguchi, T., & Randall, D. A. (2008). Large-eddy simulation of evaporatively driven entrainment in cloud-topped mixed layers. *Journal of the Atmospheric Sciences*, *65*(5), 1481–1504. https://doi.org/10.1175/2007JAS2438.1

Zhang, M., Bretherton, C. S., Blossey, P. N., Austin, P. H., Bacmeister, J. T., Bony, S., et al. (2013). CGILS: Results from the first phase of an international project to understand the physical mechanisms of low cloud feedbacks in single column models. *Journal of Advances in Modeling Earth Systems*, *5*(4), 826–842. https://doi.org/10.1002/2013MS000246